Supporting Information

**Hydrogel- and Organohydrogel-based Stretchable, Ultrasensitive, Transparent, Room-temperature and Real-time NO₂ Sensors and the Mechanism**

Yaoming Wei[a], Hao Wang[a], Qiongling Ding[a], Zixuan Wu[a], He Zhang[b], Kai Tao[c], Xi Xie[a] and Jin Wu[a]*

Yaoming Wei and Hao Wang contributed equally to this work.


[a]State Key Laboratory of Optoelectronic Materials and Technologies and the Guangdong Province Key Laboratory of Display Material and Technology, School of Electronics and Information Technology, Sun Yat-sen University, Guangzhou 510275, China

E-mail: wujin8@mail.sysu.edu.cn


[b]National Engineering Research Center of Novel Equipment for Polymer Processing, Key Laboratory of Polymer Processing Engineering (SCUT), Ministry of Education, South China University of Technology, Guangzhou, 510641, China.


[c]Ministry of Education Key Laboratory of Micro and Nano Systems for Aerospace, Northwestern Polytechnical University, Xi'an 710072, China
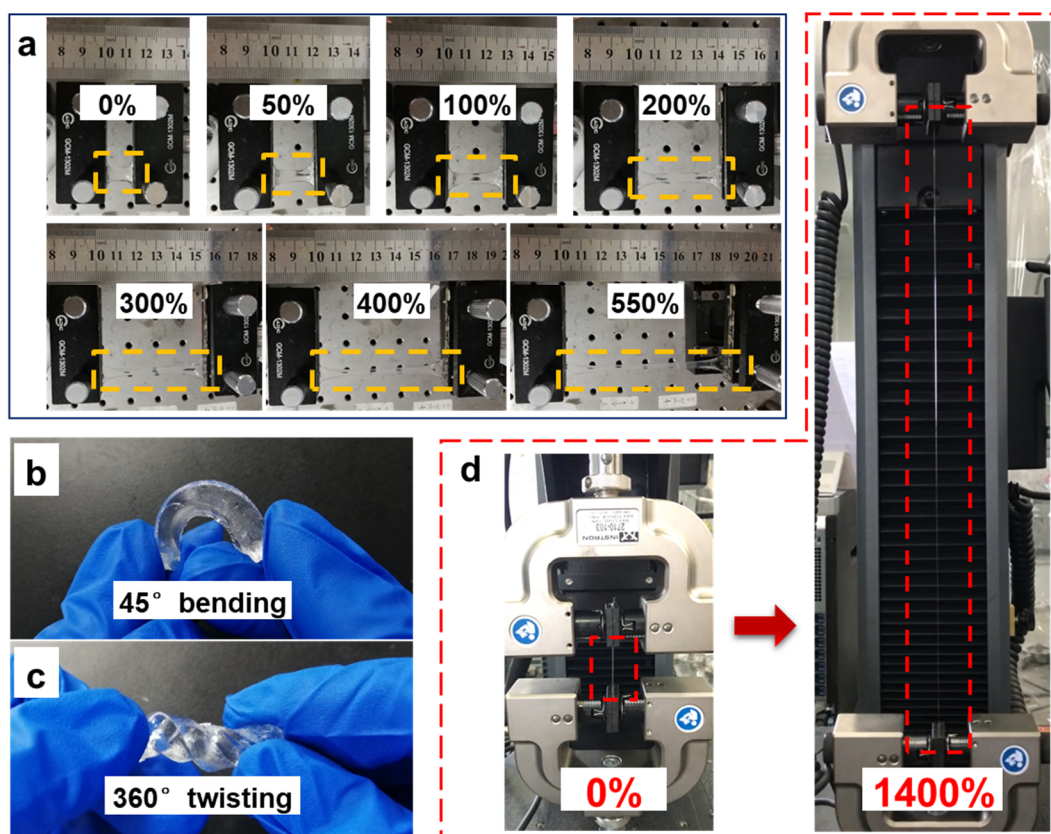
**Fig. S1** The photographs showing the DN hydrogel withstands (a) a series of tensile strains from 0% to 550%, (b) 45° bending strain, (c) 360° twisting strain and (d) 1400% tensile strain.
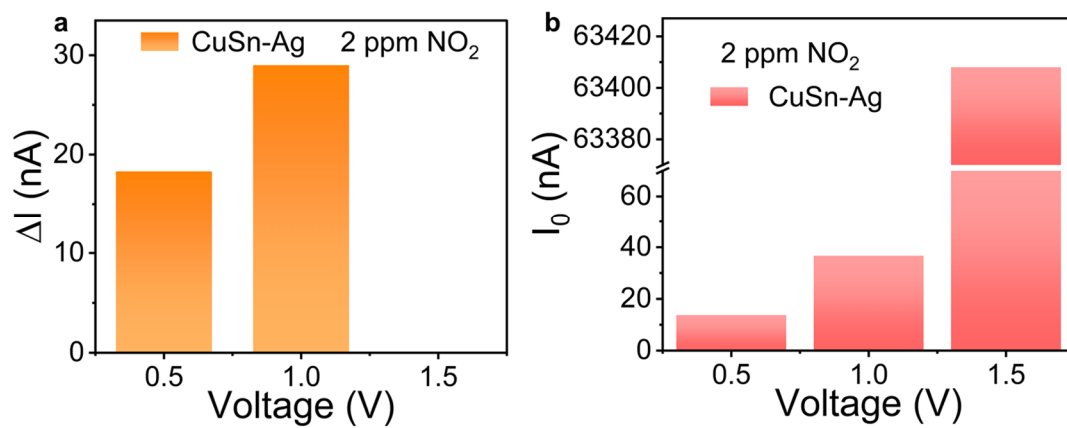
**Fig. S2** The current change $\Delta I$ (a) and base current $I_0$ (b) of the CuSn-Ag sensor in response to 2 ppm $NO_2$ at the bias voltages of 0.5, 1.0 and 1.5 V.

**Calculation of the limit of detection (LOD).**

The calculation of LOD was executed by equations S1 and S2. The procedure was as follow:

1.  Execute the 5th order polynomial fit for the baseline of response versus time curve before exposure to $NO_2$ (Fig. S3).

2.  Extract $N = 11$ data points ($Y_i$) from the baseline.

3.  Calculate the noise according to equation S1.

4.  Extract the sensitivity (slope) from the response versus the time curve (Figure 4c).

5.  Calculate the LOD according to equation S2.

$$Noise = \sqrt{\frac{\sum(Y-Y_i)^2}{N-1}}$$ (Equation S1)

$$LOD = \frac{3 \times Noise}{Slope}$$ (Equation S2)
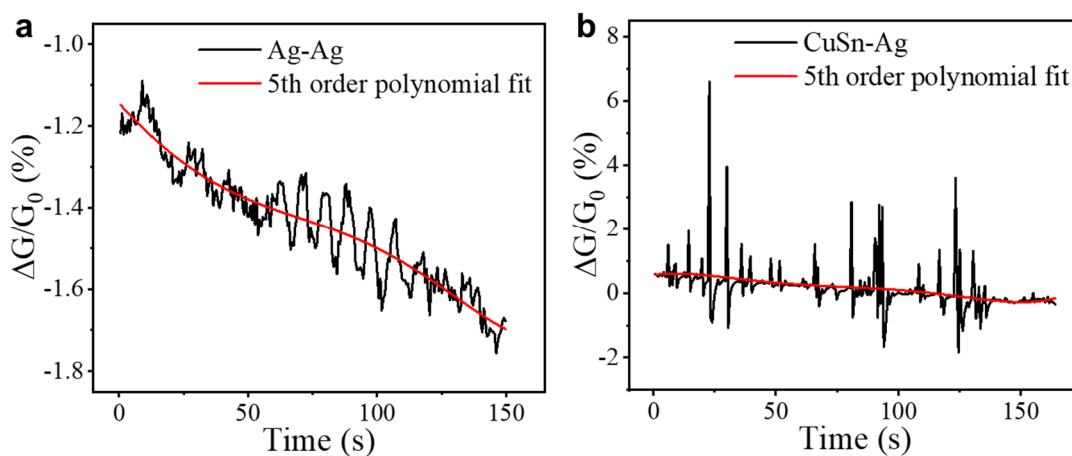


**Fig. S3** (a) and (b) The 5th order polynomial fitted results for the background responses of Ag-Ag and CuSn-Ag sensors, respectively, before exposure to $NO_2$.

**Table S1**. 5<sup>th</sup> order polynomial fitting data for the Ag-Ag $NO_2$ sensor.

| Time(s) | $Y_i$ | Y | $(Y_i-Y)^2$ |
|---|---|---|---|
| 0.59082 | -1.21781 | -1.14853 | 0.0048 |
| 10.7749 | -1.12336 | -1.21423 | 0.00826 |
| 20.35986 | -1.26956 | -1.26761 | 3.80E-06 |
| 30.54395 | -1.29414 | -1.31461 | 4.19E-04 |
| 40.729 | -1.33393 | -1.35222 | 3.34E-04 |
| 50.91309 | -1.39506 | -1.38211 | 1.68E-04 |
| 60.49805 | -1.3789 | -1.40537 | 7.01E-04 |
| 70.68213 | -1.3197 | -1.42758 | 0.01164 |
| 80.86621 | -1.3679 | -1.45 | 0.00674 |
| 90.45117 | -1.41707 | -1.47362 | 0.0032 |
| 100.63623 | -1.62214 | -1.50327 | 0.01413 |

5

**Table S2**. 5th order polynomial fitting data for the CuSn-Ag $NO_2$ sensor.

| Time(s) | $Y_i$ | Y | $(Y_i-Y)^2$ |
|---|---|---|---|
| 0.58984 | 0.58415 | 0.56492 | 3.70E-04 |
| 10.77393 | 0.45332 | 0.5984 | 0.02105 |
| 20.95801 | 0.25835 | 0.55044 | 0.08532 |
| 30.54297 | -1.07907 | 0.47352 | 2.41055 |
| 40.72705 | 0.17063 | 0.38716 | 0.04689 |
| 50.91211 | 0.2284 | 0.31236 | 0.00705 |
| 60.49707 | 0.23498 | 0.25763 | 5.13E-04 |
| 70.68115 | 0.14578 | 0.21377 | 0.00462 |
| 80.26611 | 0.14961 | 0.17914 | 8.72E-04 |
| 90.4502 | 1.68626 | 0.1398 | 2.39154 |
| 100.63379 | -0.00948 | 0.08837 | 0.00957 |

**Table S3**. Calculated noises and LODs for the Ag-Ag and CuSn-Ag $NO_2$ sensors.

| Sensor | Noise (%) | Sensitivity (%ppm$^{-1}$) | LOD (ppb) |
|---|---|---|---|
| Ag-Ag | 0.0701 | 31.18 | 6.8 |
| CuSn-Ag | 0.7354 | 60.02 | 36.8 |

6

**Table S4.** Performance comparison of various $NO_2$ sensing materials in terms of sensitivity, response/recovery time, working temperature, LOD, deformability and transparency.

| Sensing materials | Sensitivity | $t_{resp}/t_{rec}$ (s) | Temp. | LOD (ppm) | Deformability | Transparency | Ref. |
|---|---|---|---|---|---|---|---|
| sulfonated rGO | 44.3 %/ppm | / | RT | 3.6 | No | No | |
| ethylenediamine-modified rGO | 15.9 %/ppm | / | RT | 0.07 | No | No | 1 |
| WO$_3$ nanoplates | 131.75@100 ppm ($R_g/R_a$) | / | 100 °C | 5 | No | No | 2 |
| Au-WO$_3$ | 28.626 /ppm ($R_g/R_a$) | 4/59 | 100 °C | <0.25 | No | No | 3 |
| rGO/ZnO | 12@50 ppb ($R_g/R_a$) | 5.1min/ 7.5min | 100 °C | 0.005 | No | No | 4 |
| chemically functionalized RGO | 2.3 %/ppm | 284/363 | RT | 0.07 | No | No | 5 |
| Au@Te | 28 /ppm ($R_a/R_g$) | 11.3 ($t_{resp}$) | RT | 0.000083 | No | No | 6 |
| WSe$_2$ nanosheets | 1.55 /ppm ($R_a/R_g$) | / | RT | 0.008 | bending | No | 7 |
| Pt-ZnO/porous RGO | 43.28 %@5 ppm | / | RT | 0.1 | 90° bending | No | 8 |
| SnO$_2$/RGO | 4.3 %/ppm | 177/260 | RT | 0.0028 | 150° bending | No | 9 |
| PPy/N-MWCNT | 24.82 %@5 ppm | 65/668 | RT | <0.25 | bending | No | 10 |
| PbS CQD | 41 %/ppm ($R_a/R_g$) | 12/37 | RT | 0.084 | 180° bending | No | 11 |
| MoS$_2$/RGO | 6 %@1 ppm | 6min/12 min | RT | 0.0044 | 20% strain | No | 12 |
| MoS$_2$ | 160 %@5 ppm | / | RT | <5 | 40% strain | No | 13 |
| rGO/ZnO | 3.349 %/ppm | 140/630 | RT | 0.0435 | 100% strain | No | 14 |
| PAM/Ca-alginate hydrogel | 60.02 %/ppm | 79.7/ 71.3 | RT | 0.0068 | 1400% strain | Yes | This work |

The $t_{resp}$, $t_{rec}$, Temp., LOD, Ref. and RT mean the response time, recovery time, temperature, limit of detection, reference and room temperature, respectively.

Fig. S4a shows the microscopic morphology of Ag electrode before undergoing long-time (6 h) sensing test toward 2 ppm $NO_2$. EDS analysis indicates that the element composition was Ag. For cathodic Ag that had undergone sensing test (Fig. S4b), its morphology was similar with the pristine Ag but O element appeared on its surface, which was ascribed to the residual hydrogel. As shown in Fig. S4c, the surface of anodic Ag that had undergone long-term sensing test showed abundant cracks, revealing that the anode was oxidized and corroded. During all the EDS analyses, the C elements resulted from the conductive adhesive tape that was utilized to immobilize samples on the supporting SEM stage.
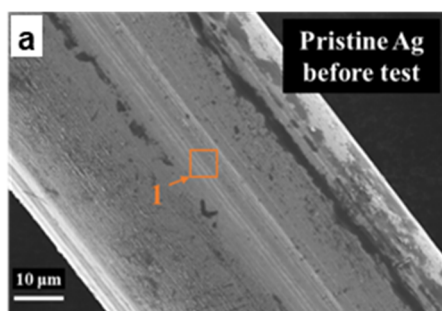


| Elements | C | O | Ag |
|---|---|---|---|
| 1 | - | - | 100.00 |

| Elements | C | O | Ag |
|---|---|---|---|
| 1 | 54.92 | 17.00 | 28.08 |
| 2 | 30.43 | - | 69.57 |

| Elements | C | Ag |
|---|---|---|
| 1 | 33.23 | 66.77 |
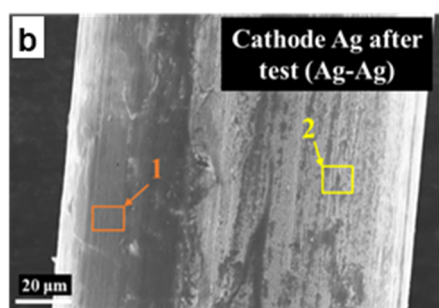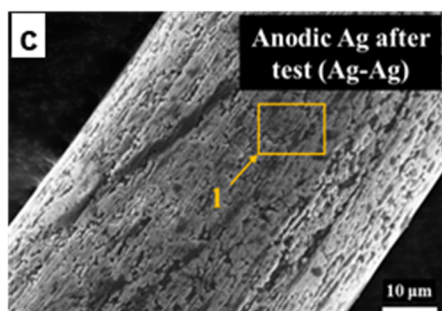
**Fig. S4** SEM images (left) and corresponding EDS results (right) of anodic and cathodic electrodes of Ag-Ag sensor before and after the continuous detection of 2 ppm $NO_2$ for

6 h. (a) The pristine Ag before sensing test. (b) The cathodic Ag after sensing test. (c) The anodic Ag after sensing test.

Fig. S5a shows the microscopic morphology of CuSn electrode before undergoing the NO$_2$ sensing test. EDS analysis shows that the atomic ratio of Cu: Sn was about 2: 1. For cathodic Ag and anodic CuSn that had undergone long-term (6 h) sensing test (Fig. S5b-c), there were obvious residual hydrogel on the surfaces and O element was observed in anode and cathode. However, different from the anode of Ag-Ag sensor (Fig. S4c), no obvious crack was detected on the anodic CuSn, presenting its superior corrosion resistance of the CuSn-Ag sensor.



| Elements | Cu | Sn |
|---|---|---|
| 1 | 67.13 | 32.87 |

| Elements | C | O | Ag |
|---|---|---|---|
| 1 | 26.09 | 2.25 | 71.66 |

| Elements | C | O | Cu | Sn |
|---|---|---|---|---|
| 1 | 50.05 | 17.32 | 23.61 | 9.02 |
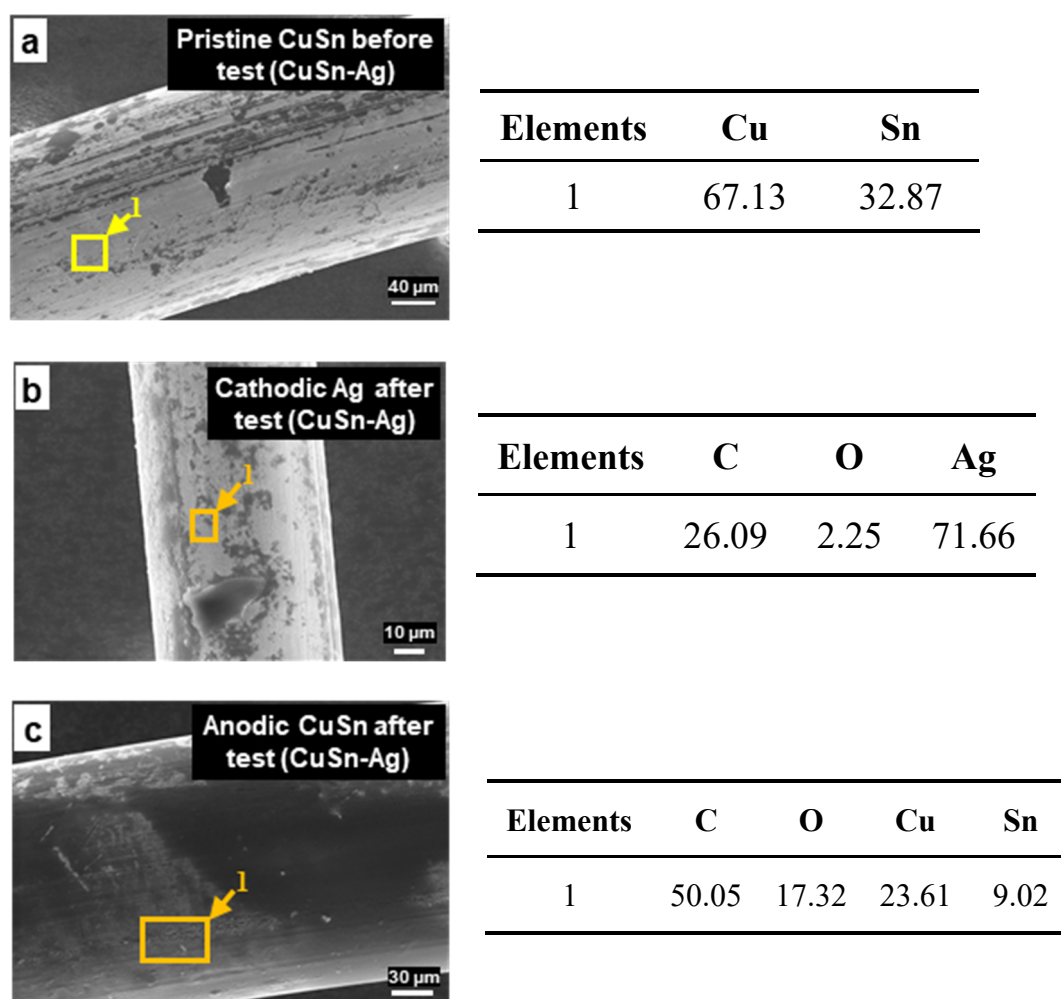
**Fig. S5**. SEM images (left) and corresponding EDS results (right) of anodic and cathodic electrodes of CuSn-Ag sensor before and after gas sensing tests toward 2 ppm NO$_2$ for 6 h. (a) The pristine CuSn before NO$_2$ sensing test. (b) The cathodic Ag after NO$_2$ sensing test. (c) The anodic CuSn after NO$_2$ sensing test.
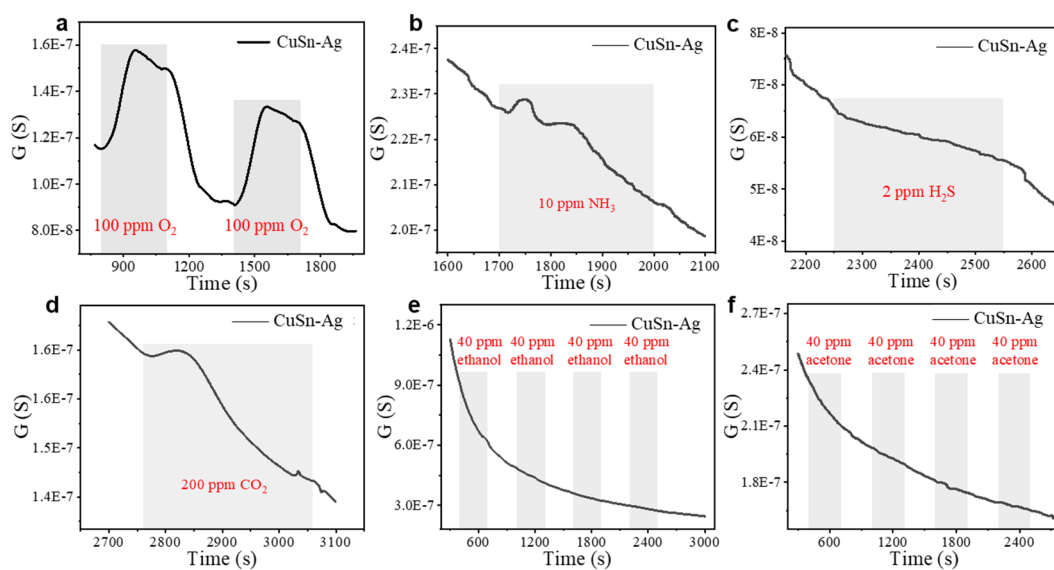
**Fig. S6**. Investigation of the selectivity of the CuSn-Ag hydrogel sensor toward $NO_2$. Time-dependent conductance change of the sensor in response to (a) 100 ppm $O_2$, (b) 10 ppm $NH_3$, (c) 2 ppm $H_2S$, (d) 200 ppm $CO_2$, (e) 40 ppm ethanol (repeated 4 cycles) and (f) 40 ppm acetone (repeated 4 cycles).
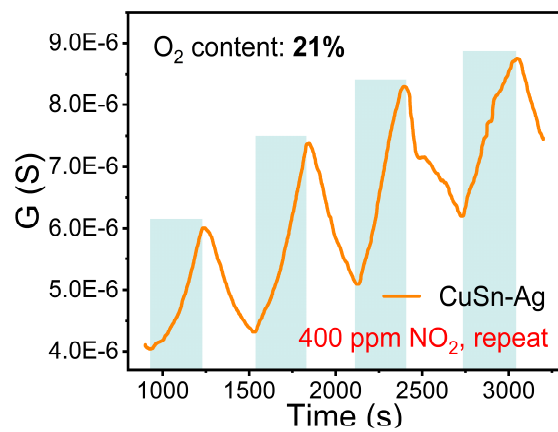
**Fig. S7**. Time-dependent conductance change of the sensor in response to 400 ppm NO$_2$ in the presence of 21% O$_2$ (air background) for repeated 4 experimental cycles.
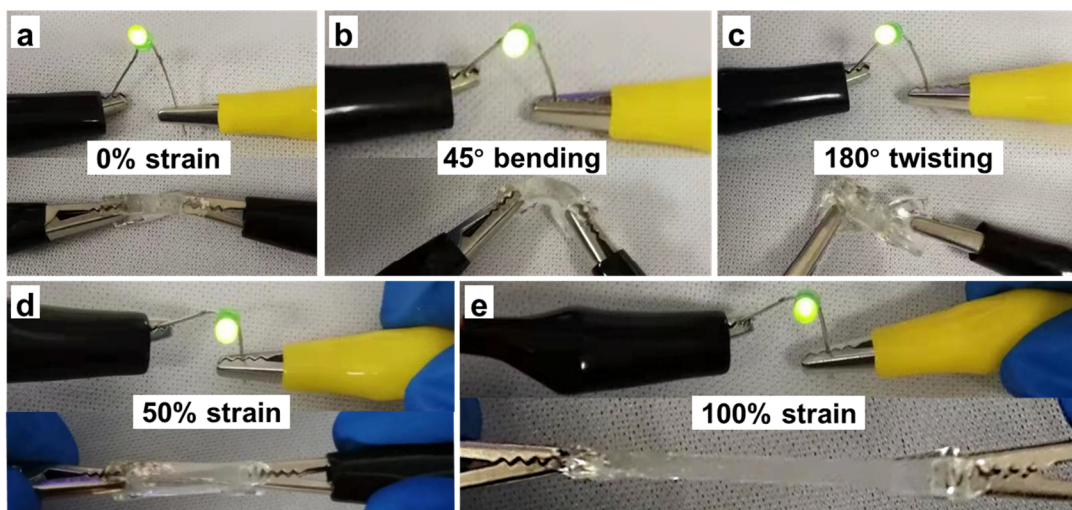
**Fig. S8**. The LED lights were lightened by a direct current power source when DN hydrogel was connected in series in the circuit. The LED light kept on when various deformations were applied to the hydrogel, including (a) 0% strain, (b) 45° bending, (c) 180° twisting, (d) 50% tensile strain, and (e) 100% tensile strain, indicating the maintained conductance.
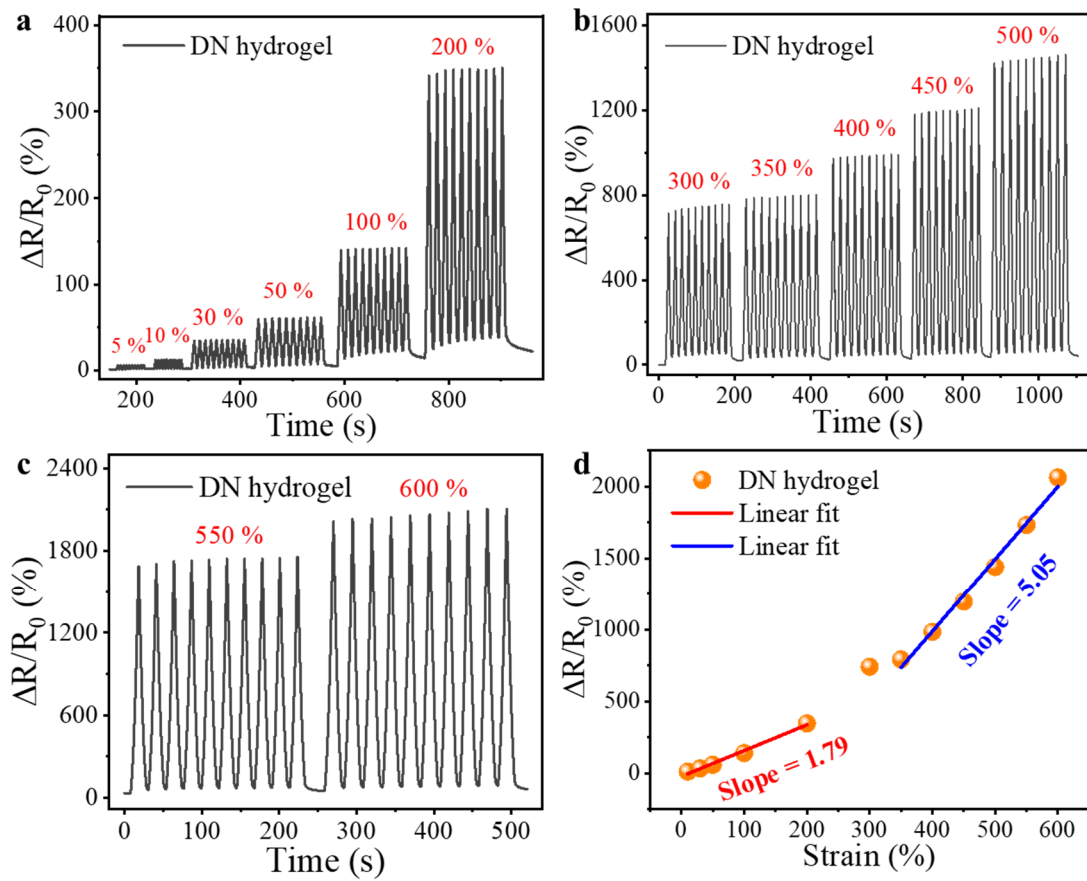
**Fig. S9**. Electromechanical response of the hydrogel sensor. (a-c) Dynamic curves showing the relative resistance changes of DN hydrogel upon loading and unloading a series of tensile strains from 5% to 600%. The strain sensing test was executed 10 times for each strain. (d) The linear fitted relative resistance changes versus strains, from which the gauge factors were deduced within different strain ranges.

**Alarm demonstration system**

The whole system consists of sensor, hardware system and software system. The hardware system is composed of voltage follower, signal conditioning circuit, power supply module, Bluetooth module, alarm module and Microprogrammed Control Unit (MCU), as shown in Fig. 7a-b. Among them, voltage follower circuit is used for stabilized output of Digital-to-Analog Converter (DAC), which ensures that the voltage at both ends of the sensor is constant. The signal output from the sensor was collected by the Analog to Digital Converter (ADC) of the MCU after passing through the signal conditioning circuit, and the data finally was sent to the user terminal via Bluetooth. Moreover, the alarm was triggered when the value collected by ADC was greater than the set value.

## References

1.    W. Yuan, A. Liu, L. Huang, C. Li and G. Shi, *Adv. Mater.*, 2013, **25**, 766-771.

2.    S. S. Shendage, V. L. Patil, S. A. Vanalakar, S. P. Patil, N. S. Harale, J. L. Bhosale, J. H. Kim and P. S. Patil, *Sens. Actuators, B*, 2017, **240**, 426-433.

3.    S. Zhao, Y. Shen, P. Zhou, X. Zhong, C. Han, Q. Zhao and D. Wei, *Sens. Actuators, B*, 2019, **282**, 917-926.

4.    J. Liu, S. Li, B. Zhang, Y. Xiao, Y. Gao, Q. Yang, Y. Wang and G. Lu, *Sens. Actuators, B*, 2017, **249**, 715-724.

5.    J. Wu, Y. Wei, H. Ding, Z. Wu, X. Yang, Z. Li, W. Huang, X. Xie, K. Tao and X. Wang, *ACS Appl. Mater. Interfaces*, 2020, **12**, 20623-20632.

6.    Z. Yuan, Q. Zhao, C. Xie, J. Liang, X. Duan, Z. Duan, S. Li, Y. Jiang and H. Tai, *Sens. Actuators, B*, 2022, **355**, 131300.

7.    C. Yang, J. Xie, C. Lou, W. Zheng, X. Liu and J. Zhang, *Sens. Actuators, B*, 2021, **333**, 129571.

8.    J.-Y. Kang, W.-T. Koo, J.-S. Jang, D.-H. Kim, Y. J. Jeong, R. Kim, J. Ahn, S.-J. Choi and I.-D. Kim, *Sens. Actuators, B*, 2021, **331**, 129371.

9.    J. Wu, Z. Wu, H. Ding, Y. Wei, W. Huang, X. Yang, Z. Li, L. Qiu and X. Wang, *ACS Appl. Mater. Interfaces*, 2020, **12**, 2634-2643.

10.   B. Liu, X. Liu, Z. Yuan, Y. Jiang, Y. Su, J. Ma and H. Tai, *Sens. Actuators, B*, 2019, **295**, 86-92.

11.   H. Liu, M. Li, O. Voznyy, L. Hu, Q. Fu, D. Zhou, Z. Xia, E. H. Sargent and J. Tang, *Adv. Mater.*, 2014, **26**, 2718-2724.

12.   N. Yi, Z. Cheng, H. Li, L. Yang, J. Zhu, X. Zheng, Y. Chen, Z. Liu, H. Zhu and H. Cheng, *Mater. Today Phys.*, 2020, **15**, 100265.

13. M. A. Islam, H. Li, S. Moon, S. S. Han, H.-S. Chung, J. Ma, C. Yoo, T.-J. Ko, K. H. Oh, Y. Jung and Y. Jung, *ACS Appl. Mater. Interfaces*, 2020, **12**, 53174-53183.

14. W. Li, R. Chen, W. Qi, L. Cai, Y. Sun, M. Sun, C. Li, X. Yang, L. Xiang, D. Xie and T. Ren, *ACS Sens.*, 2019, **4**, 2809-2818.